Supporting Information

An electrochemical oscillator for harvesting near room temperature waste heat

Basanta Ghimire [1,2†], Mihir Parekh [1,2*†], Herbert Behlow [1,2], Morteza Sabet [2,3], Sriparna Bhattacharya [1,2], Nawraj Sapkota [1,2], Pankaj Singh Chauhan [4], Abha Misra [4], Apparao M. Rao [1,2*]

[1] Department of Physics and Astronomy, Clemson University, 118 Kinard Laboratory, Clemson, South Carolina, USA
[2] Clemson Nanomaterials Institute, Clemson University, 81 Technology Drive, Anderson, South Carolina, USA
[3] Department of Automotive Engineering, Clemson University, 4 Research Dr, Greenville, South Carolina, USA
[4] Department of Instrumentation and Applied Physics, Indian Institute of Science, Bengaluru, Karnataka, India

*Corresponding authors: mihirp@clemson.edu and arao@clemson.edu

Contributing authors: basantg@clemson.edu; hbehlow@clemson.edu; ssabet@clemson.edu; nsapkot@clemson.edu; bbhatta@g.clemson.edu; pschauhan.89@gov.in; abha@iisc.ac.in
†These authors contributed equally to this work.

This file contains the methods section, supplementary figures, FFT analysis data, and details of the developed model and testing with constant resistance load. Downloadable supplementary movies are also included.

Table of Contents

Methods

Delignification process

Balsa wood sheets with a thickness of 1.5 mm were purchased from Amazon, USA. The matrix substances, such as lignin and hemicellulose, were removed following the procedure reported in our previous work[1,2]. The wood pieces were boiled in a 2% sodium chlorite solution buffered with acetic acid at pH 4.6. The solution was changed every 6 hours, and the reaction was continued until white delignified wood (DW) was attained after 4 days. The DW pieces were washed thoroughly with DI water and freeze-dried using a FreeZone freeze-dry system (Labconco, MO, USA). The scanning electron micrographs and Fourier-transform infrared (FTIR) characterization data of the cellulosic separator obtained from DW are shown in Fig. S2.

Coin cell preparation

The cellulosic separator obtained from DW was further treated before being used in our coin cells. It was soaked overnight in an aqueous solution of 0.28 M sodium chlorite containing 20 wt% polyethylene oxide. Symmetric coin cells, shown in Fig. 1a, were fabricated using three types of porous electrodes: (i) Bucky Paper (60 $g\,m^{-2}$) made from multi-walled carbon nanotubes (MWCNTs) purchased from NanoTechLabs (NC, USA), (ii) high-porosity aluminum foil # 071375 (type CD1), and (iii) low-porosity aluminum foil # 140012 (type CD2). Both CD1 and CD2 anodized aluminum oxide (AAO) foils were obtained from Cornell Dubilier Electronics (SC, USA).

TRECO module fabrication

A module was fabricated comprising four TRECO coin cells (20 mm diameter) connected electrically in series but thermally in parallel between two copper heatsinks. Because the heatsinks in the setup must provide ΔT, an electrically insulating layer was used to connect the cells in series. We used pouch-cell metalized polymer film (~100 mm x ~100 mm x ~0.1 mm) as the electrically insulating layer upon which we placed four conductive pads made from adhesive-backed Cu tape (~25 mm dia. x 0.1 mm thickness) arranged in a square (Fig. 8a). A second insulating layer with four similarly placed Cu pads was constructed for placement against the opposing heatsink, such that the TRECO cells could be sandwiched between matching opposite Cu pads. Electrical connections were made by soldering a polymer-insulated #30 AWG Cu wire to the edge of the Cu pads, providing a series circuit of the four TRECO coin cells.

Characterizations

Fourier-transform infrared spectroscopic analysis was conducted directly on wood sheets (before and after delignification) with a ThermoFisher Nicolet iS50 spectrometer equipped with a diamond ATR. Scanning electron microscopy (SEM) examinations were carried out using a Hitachi SU6600 FE-SEM at 5 kV. Gas physisorption measurements were conducted on porous electrodes using a Quantachrome Autosorb iQ gas sorption analyzer using N_2 gas.

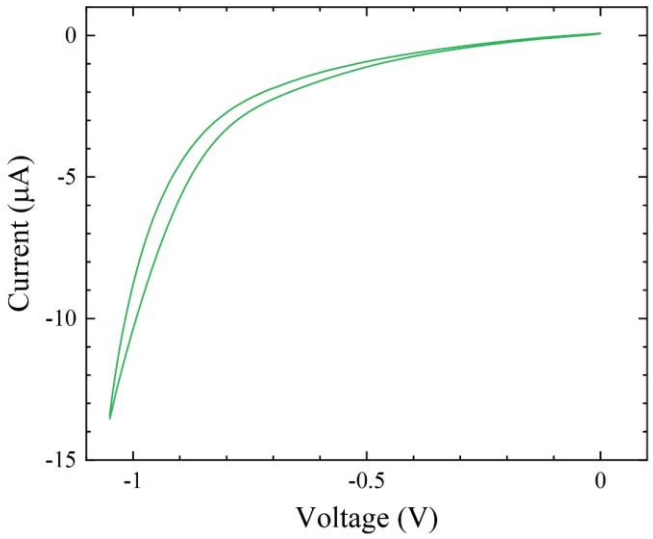

Figure S1: Cyclic Voltammetry plot of a symmetric TRECO cell with CD1 electrodes. No discernable redox peaks are present. In fact, the CV curve is similar to that of a memristor.[3,4]

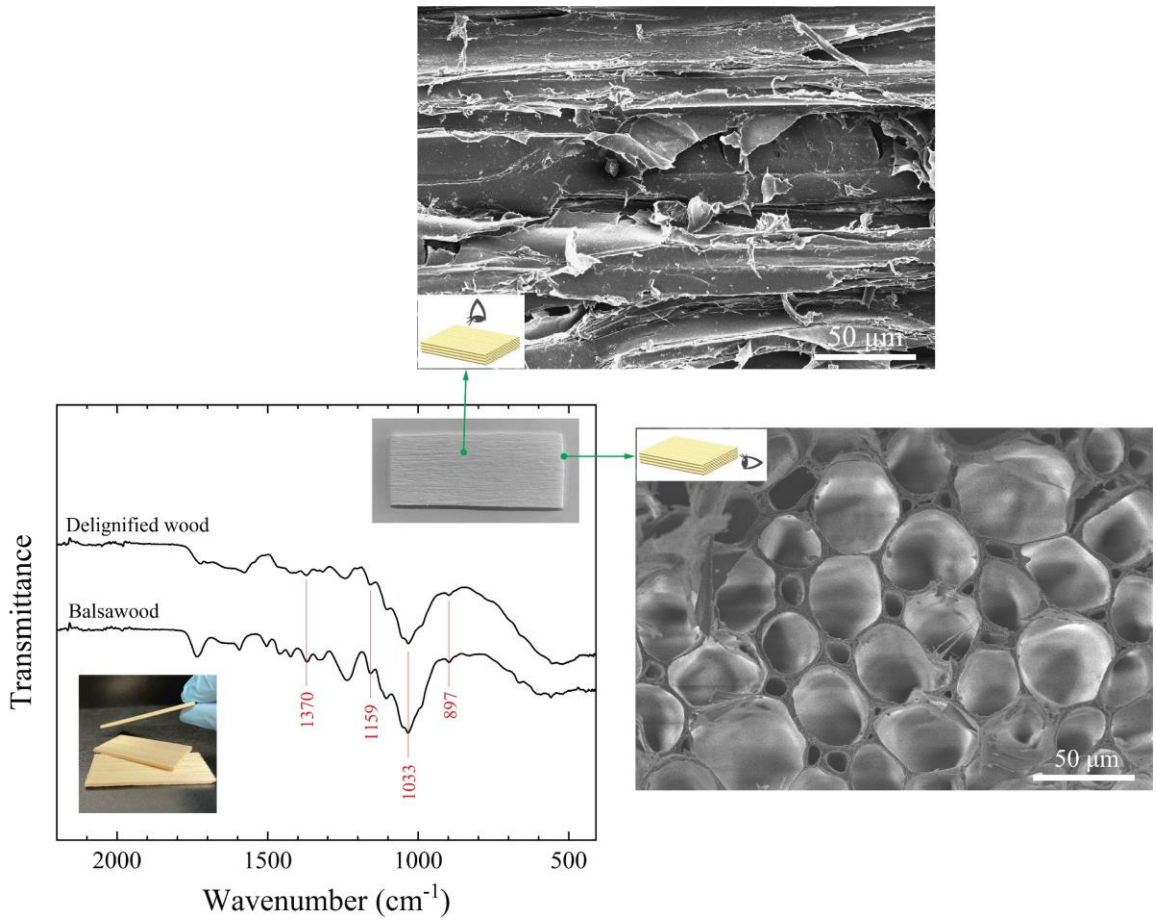

Figure S2: Characterization data for deliginified wood-based cellulose separator showing SEM micrographs of a cross-section (top), Fourier-Transform Infrared Spectroscopy data (FTIR) data (bottom left), SEM of the top view (bottom right). SEM micrographs indicate the orientation of wood cells (fibers). The characteristic IR peaks for cellulose (labeled in red) are detected after the delignification process.

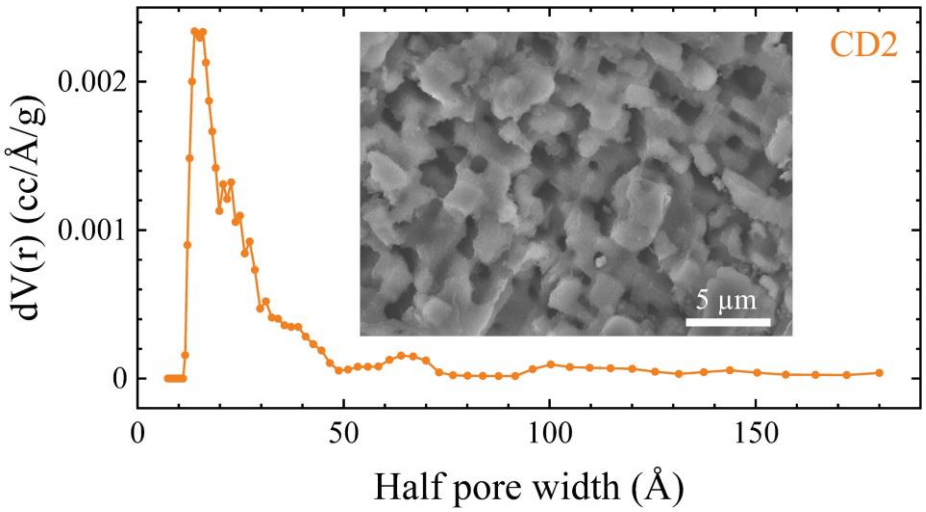

Figure S3: Density functional theory (DFT)-based pore size distribution of CD2 electrode. The inset shows an SEM micrograph of the CD2 electrode's surface.

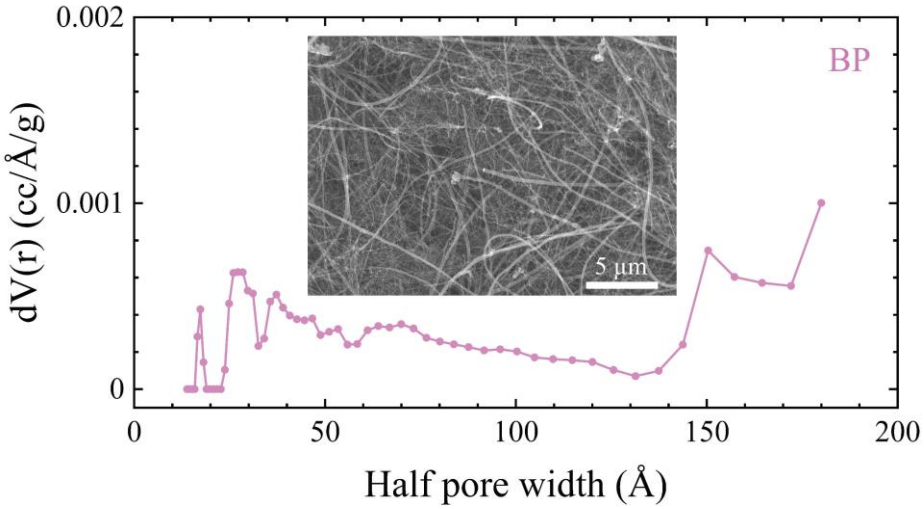

Figure S4: Density functional theory (DFT)-based pore size distribution of BP electrode. The inset shows an SEM micrograph of the BP electrode's surface.

Table S1: Maximum open circuit voltages for multiple TRECO cells based on CD1, CD2, and BP electrodes

Cell number	Electrode type		
	CD1	CD2	BP
1	-0.74 V	-0.79 V	-0.63 V
2	-0.83 V	-1.11 V	-0.67 V
3	-1.18 V	-0.79 V	-0.45 V
4	-0.84 V	-1.26 V	
5	-1.02 V	-1.06 V	
Average +/- S.D.	-0.922 V +/- 0.176 V	-1.002 V +/- 0.207 V	-0.5833 V +/- 0.117 V

Factors to consider while choosing separator material

(a) It should be a poor thermal conductor to reduce heat conduction from the hot electrode to the cold electrode.

(b) It should be a poor electronic conductor to prevent an internal short circuit.

(c) It should be wettable by the electrolyte.

(d) It should be porous to soak up the electrolyte; ideally, the channels (pores) within the separator must be open and normal (oriented perpendicularly) to the electrodes. As per the IUPAC definition, closed pores do not run from one end to the other but are terminated by solid material somewhere in between. Such pores will hinder ionic movement and affect the cell's electrical performance.[5]

Factors to consider while choosing the electrolyte material

The chosen electrolyte should be such that

(i) It wets the electrode and the separator

(ii) There is a significant difference in thermodiffusivity between the oppositely charged ions

The synergy between electrolyte and separator improves thermopower

It is desirable that the same ion (whose movement is favored by the separator and has higher thermodiffusivity) also has higher diffusivity. This is because, in Soret-effect driven cells, the voltage is generated by charge separation, achieved due to differences in ionic thermodiffusivities and/or ionic diffusivity. Since thermodiffusivity is an ionic property that depends upon the temperature, solvent, salt concentration, etc., proper salt/solvent and concentration choice for a given operating temperature is important. However, the thermopower can be enhanced if the chosen separator is selectively permeable to the ion with a higher thermodiffusivity. This will ensure that charge separation is higher because all the 3 factors, viz., (a) the applied temperature gradient, (b) the chosen separator, and (c) ionic diffusivity differences, favor the movement of one ion over the other.

Effect of porosity on the heat of transport (Q^*)

The heat of transport (Q^*) is an inherent property of an ion that depends on temperature, solvent, salt concentration, etc. Hence, Q^* is largely unaffected by porosity. However, if the pore sizes are comparable to the ion's solvation shell size, then ion confinement effects could affect Q^*. Because we do not expect a significant temperature gradient within the tiny electrode pores (which are a few nm in dimension, as can be seen from Figs. 1c, S1, and S2), theromodiffusion is largely negligible inside the pores, emphasizing that the electrode porosity should not affect Q^* or the cell performance drastically. Given that the cellulosic separator is also hierarchically porous, Q^* of both ions will be affected, and an effective heat of transport akin to effective diffusivity[6,7] for porous materials (which depends on the porosity and tortuosity) might be better suited for analysis. This topic is under further investigation, which we hope to report in our future publications.

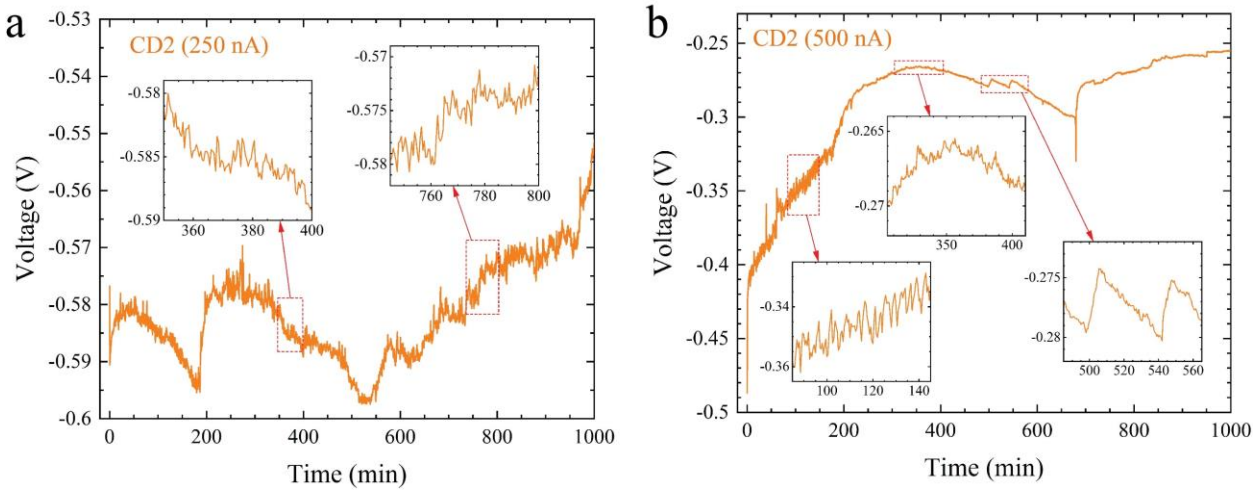

Figure S5: Temporal voltage profile of a TRECO cell based on CD2 electrodes, cellulose obtained from delignified wood as the separator, and an aqueous electrolyte containing sodium chlorite and polyethylene oxide for (a) 250 nA discharge current, and (b) 500 nA discharge current. All data was obtained for a temperature difference of 10 °C across the two electrodes.

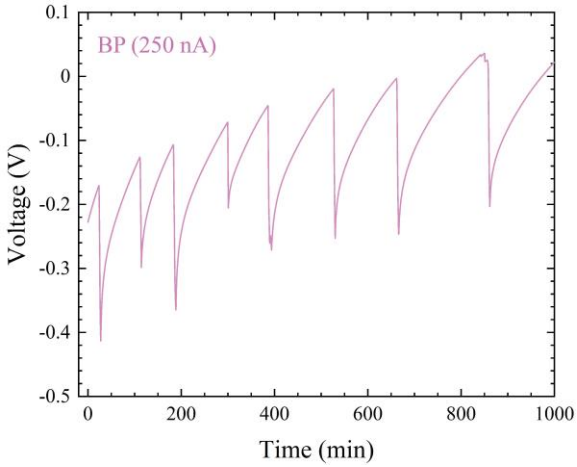

Figure S6: Temporal voltage profile of a TRECO cell based on BP electrodes, cellulose obtained from delignified wood as the separator, and an aqueous electrolyte containing sodium chlorite and polyethylene oxide for 250 nA discharge current. All data was obtained for a temperature difference of 10 °C across the two electrodes.

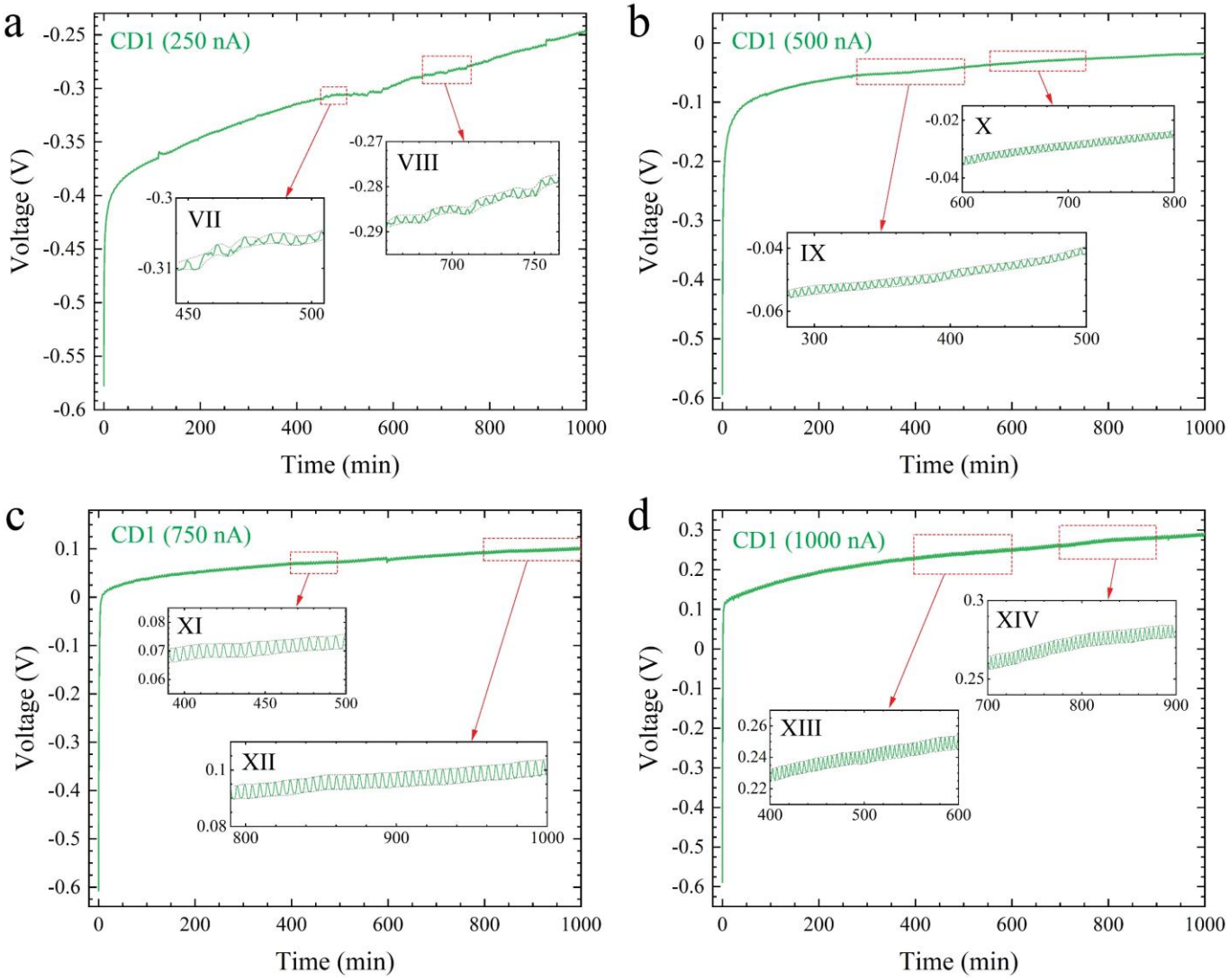

Figure S7: Temporal voltage profile of a TRECO cell based on CD1 electrodes (housed in a stainless setup instead of copper setup), cellulose obtained from delignified wood as the separator, and an aqueous electrolyte containing sodium chlorite and polyethylene oxide for (a) 250 nA, (b) 500 nA, (c) 750 nA, (d) 1000 nA discharge current. All datasets were obtained for a temperature difference of 7.5 K across the two electrodes. In each of the insets, a gray colored dotted line joining all the peaks and the valleys has been added as a guide to the eye to enable the reader to observe low-frequency oscillations. The very regular oscillations arise from PID controller-induced temperature fluctuations, but there are other long time-period oscillations as well, apart from the PID controller-induced oscillations.

To track the temperature variations associated with the PID controller, we fabricated a separate setup using stainless steel instead of copper. Copper's thermal conductivity is ~400 W/(m.K)[8] and that of stainless steel is ~15 W/(m.K). [9] The low thermal conductivity of stainless steel increases the time lag between temperature sensing and the variation in the current passing through the heater embedded inside the setup. In case of copper, the time lag is negligible, but in case of stainless steel, the time lag is roughly 5 minutes (implying that the temperature difference fluctuates between 7.3 K to 8 K for a set temperature difference of 7.5 K Hence, when the stainless steel setup is used, the ΔT oscillates in 5-minute intervals in sync with the PID controller (SM2) (this can be seen by observing the 'short term voltage trace' and the temperature fluctuation in (SM2). This large time lag provides the ions sufficient time to diffuse through the electrolyte in response to the temperature fluctuation, and hence voltage oscillations during discharge, show a '5 minute time period (frequency ~ 0.003 Hz)' associated with this fluctation, along with other frequencies related to system dynamics (interplay of Fick's diffusion and ionic migration within the electric double-layer at the electrode-electrolyte interfaces). The presence of other frequencies makes it clear that PID controller-induced temperature variations are not the sole cause for voltage oscillations.

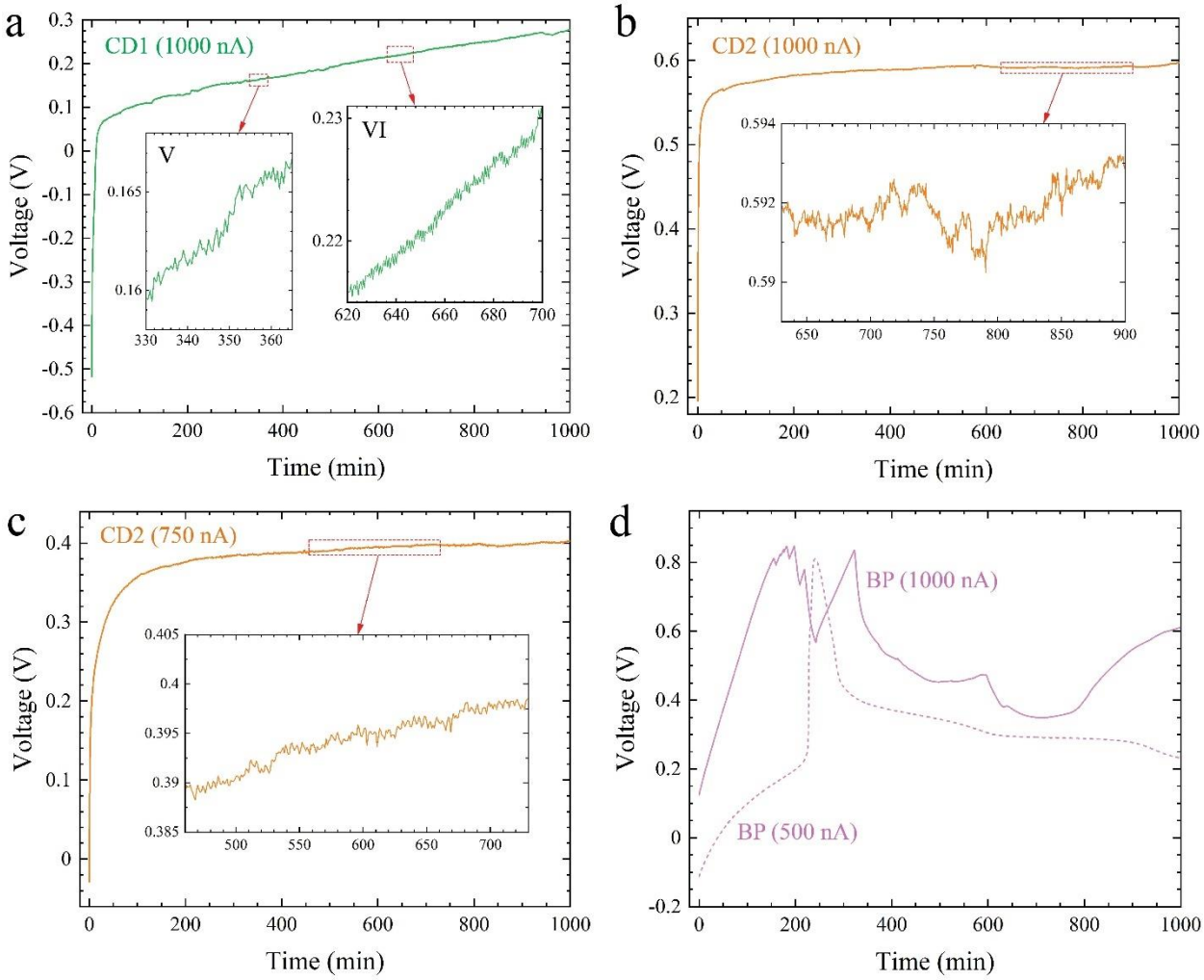

Figure S8: Temporal voltage profile of a symmetric cell based on (a) CD1 and (b) CD2 electrodes with 1000 nA discharge current. Panel (c) depicts the voltage profile for symmetric cells based on CD2 electrodes at 750 nA current, and panel (d) shows the temporal voltage profile for symmetric cells with BP electrodes at 500 nA (dotted line), and 1000 nA (solid line). A cellulosic separator (described in the Methods section) was used in our cells. Additionally, an aqueous electrolyte containing sodium chlorite and polyethylene oxide was used. All the data was obtained for a temperature difference of 10 °C across the two electrodes.

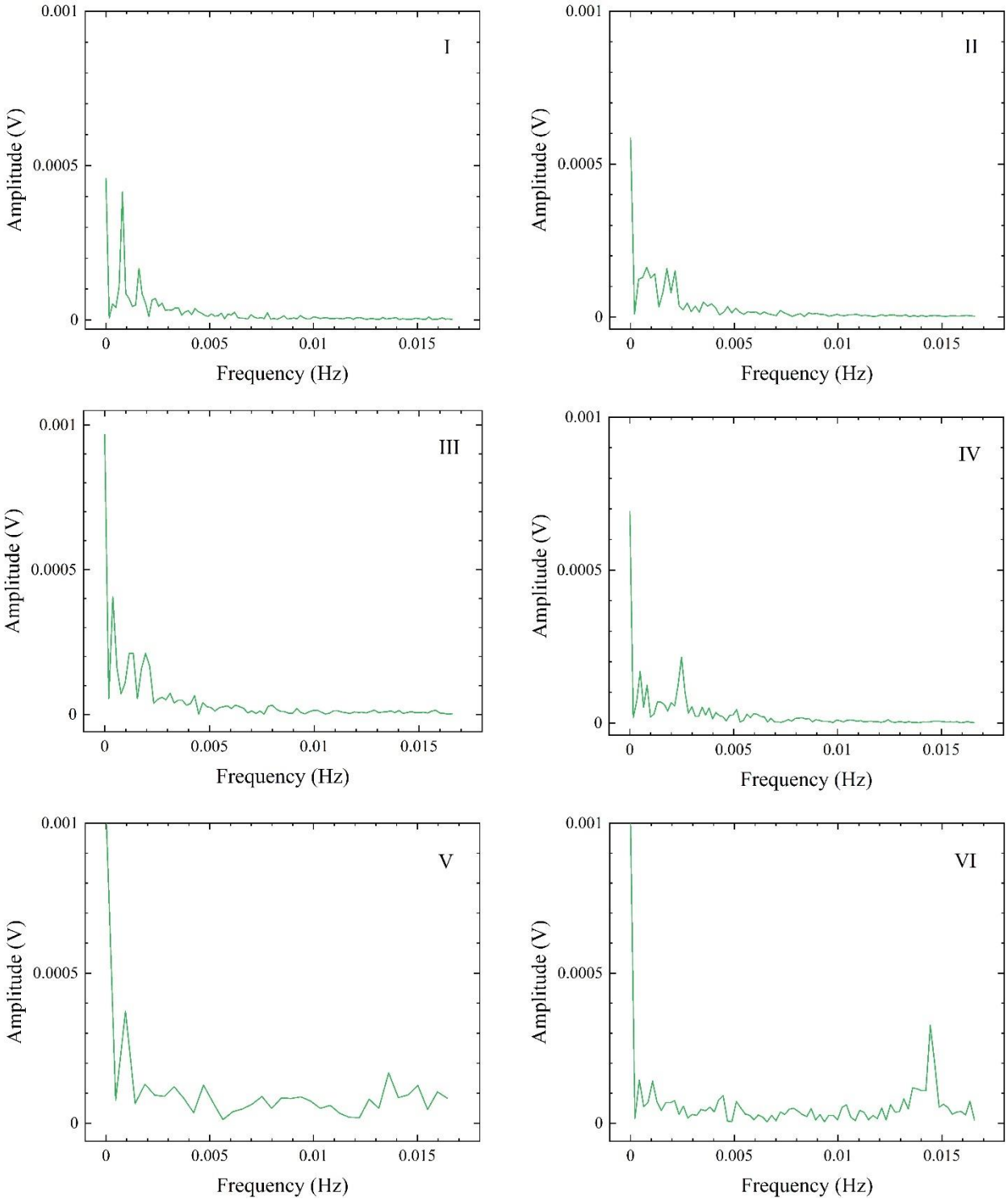

Figure S9: Fast Fourier transform of insets I-VI in Figs. 3 and S8a.

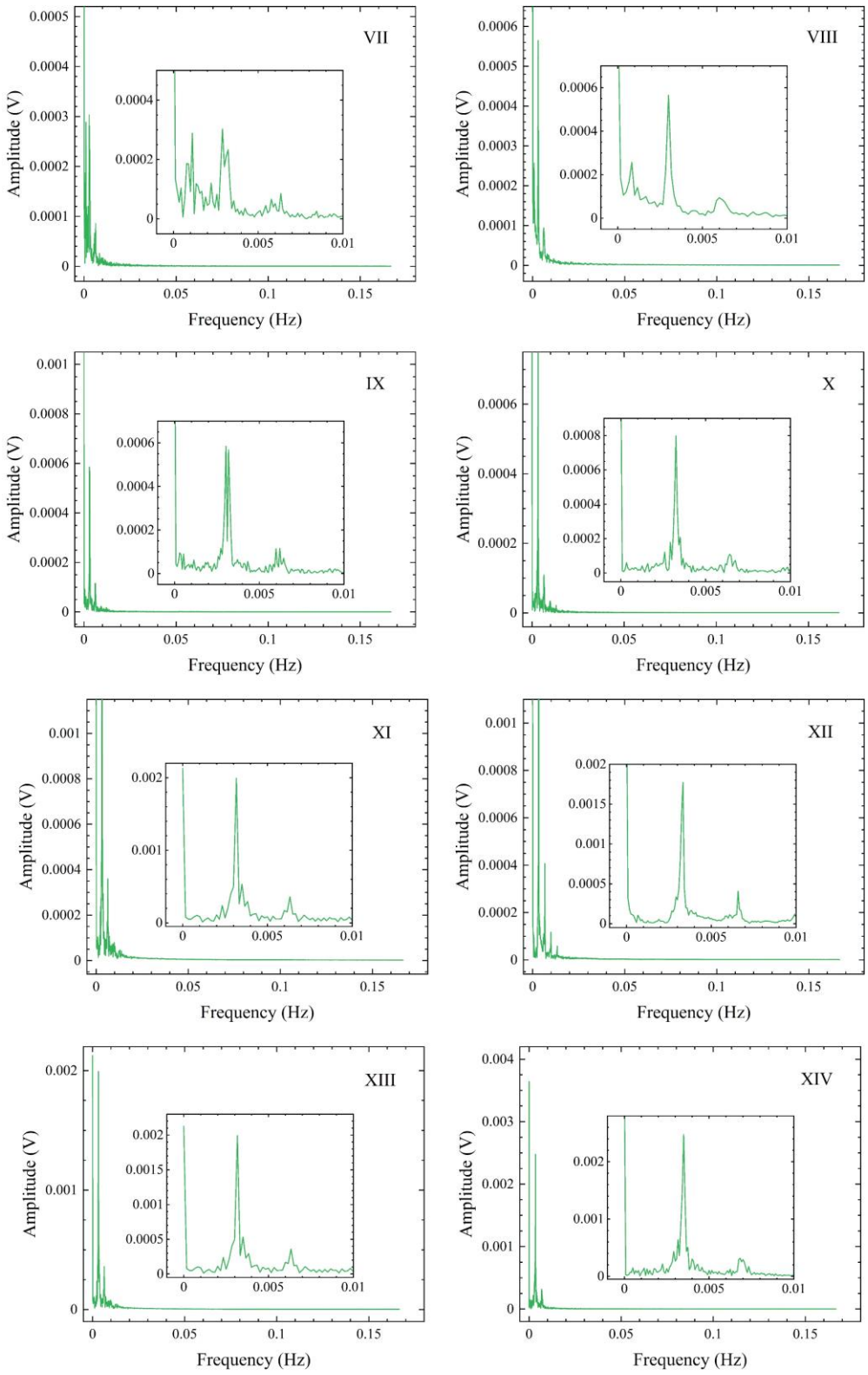

Figure S10: Fast Fourier transform of insets VII-XIV in Fig. S7.

Table S2: A summary of the results obtained from the fast Fourier transform (FFT) analysis of insets I – VI in Figs. 3 and S5a (ΔT = 10 K, copper setup, CD1 electrodes).

Current (nA)	Time (mins)	Frequency Range (mHz)	Peak Amplitudes (mV)
250 - Inset I	205-310	0.79-2.53	0.207 - 0.022
250 - Inset II	820-905	0.779-4.67	0.081 - 0.0169
500 - Inset III	465-550	0.38-4.28	0.202 - 0.032
500 - Inset IV	850-950	0.49-5.97	0.084 - 0.015
1000 - Inset V	330-365	0.93-16.43	0.186 - 0.084
1000 - Inset VI	620-698	1.06-16.34	0.16 - 0.025

Table S3: A summary of the results obtained from the fast Fourier transform (FFT) analysis of insets VII – XIV in Fig. S7 (ΔT = 7.5 K, stainless steel setup, CD1 electrodes). The frequencies in red are attributed to the PID controller-induced fluctuations, and the ones in blue are likely overtones of the PID controller-induced fluctuations.

Current (nA)	Time (mins)	Frequencies (mHz)
250 – Inset VII	450-500	0.44, 0.77, 0.88, 1.11, 1.44, 1.66, 2.22, 2.88, 3.22, 3.55, 5.77, 6.33
250 – Inset VIII	660-760	0.833, 1.17, 1.67, 2.17, 2.5, 3, 6
500 – Inset IX	280-500	0.53, 2.57, 2.72, 3.02, 3.18, 6.21
500 – Inset X	550-750	2.92, 3.25, 3.5, 6.42
750 – Inset XI	395-495	2.83, 3.17, 3.5
750 – Inset XII	800-1000	2.92, 3.33, 6.58
1000 – Inset XIII	400-600	2.83, 3.08, 3.33, 3.5, 3.67, 3.83
1000 – Inset XIV	700-900	2.92, 3.17, 3.5, 3.75, 6.83

Discussion about FFT data:

Firstly, a third-order polynomial was fitted to the data presented in the insets I – VI of Figs. 3 and S7a. For insets VII – XIV of Fig. S6, a ninth-order polynomial was used for fitting. The data was then subtracted from the fitted polynomial to perform background correction. Next, the minimum point in the data obtained after the previous step was shifted to zero. Henceforth, we refer to this newly obtained data as 'background corrected data'. Subsequently, a one-sided fast Fourier transform of the 'background corrected data' was performed, and the results were normalized. The normalization factor was chosen to be 1/(Sampling interval*number of samples). The normalized results are shown in Figs. S9 and S10, where the voltage amplitude at 0 Hz represents the average value (DC value) of the 'background corrected' time domain data.

Figures S9 and S10 suggest that voltage oscillations in each inset have multiple frequency components (with different phase shifts). While components at certain frequencies have larger amplitudes, there are many frequencies with smaller amplitudes, too. To focus on the dominant frequencies, we looked at the frequencies whose amplitude was at least 10% of the amplitude of the most dominant non-zero frequency. A comparison of Figures S9 and S10 (at all currents) suggests that for both ΔT= 7.5 K and ΔT=10 K, there are peaks around or before 1 mHz, which seems to be the common oscillation frequency associated with the system dynamics, irrespective of the temperature and setup. This is expected because our derivations, presented in the main manuscript and the SI, have shown that the Soret effect does not affect the oscillations directly.

Table S2 suggests that for all the currents used in this study, the inset taken at an earlier time interval has a larger spread of peak amplitudes in the FFT data (shown in Fig. S9). Nonetheless, the frequency spread is larger for the later inset, irrespective of the current. Additionally, the number of peaks is also larger for later insets. Since (a) we have more peaks (or more frequency components) in later insets and (b) the voltage oscillation amplitude is roughly the same (in the time domain), the contribution of individual frequency components to the oscillations will be reduced. This explains the smaller spread of peak amplitudes for later insets. Lastly, fewer peaks in the earlier insets at all the currents imply that ions within larger pores probably start contributing to the oscillations earlier than ions within smaller pores. This is because several smaller pores may

be connected to larger pores (as in a hierarchically porous structure wherein micropores and mesopores are present inside macropores).

On the contrary, Table S3 (ΔT = 7.5 K and stainless steel setup) suggests that the number of frequencies at an earlier inset is higher than that at a later inset. This behavior is different from the behavior with ΔT = 10 K and copper setup (represented in Table S2). A possible explanation for this behavior could be the fact that at 7.5 K, the voltage is lower, so most of the ions possibly only fill the larger pores in the hierarchical porous structure, and hence, their contribution to oscillations starts to reduce once they are out of the pores due to TRECO being discharged.

While, at a fixed current, the frequencies are expected to be characteristic of the material's microporous structure, the complexity of the porous structure (hierarchically porous structure with pores of multiple sizes) leads to different FFT plots for two separate insets at the same current. However, we expect a single dominant frequency for a fixed current for an electrode with a uniform porous structure (with a narrow pore size distribution). Moreover, the frequencies in the range of mHz indicate that the period of oscillation is of the order of several minutes, as evident in the time domain data.

Estimation of time-scales for Fick's diffusion and thermodiffusion

Order of magnitude for Fick's diffusion

Equation 1 suggests that the time-scale of Fick's diffusion can be calculated as follows:

$$\frac{\partial C_i}{\partial t} \sim \frac{\partial (D_i \frac{\partial C_i}{\partial x})}{\partial x}$$

which implies

$$\frac{C_i}{t} \sim \frac{D_i C_i}{L^2}$$

Thus, the time-scale 't' for Fick's diffusion of species i is given by $t \sim \frac{L^2}{D_i}$, where 'L' is the distance between two electrodes. Using L as 1 mm and typical D ~ 1E-9 m^2/s gives t ~1000 s.

Order of magnitude for thermodiffusion

Equation 1 suggests that the time-scale of thermodiffusion can be calculated as follows:

$$\frac{\partial C_i}{\partial t} \sim \frac{\partial (\frac{D_i Q_i^* C_i \frac{\partial T}{\partial x}}{k_b T^2})}{\partial x}$$

which implies

$$\frac{C_i}{t} \sim \frac{D_i Q_i^* C_i T}{k_b T^2 L^2}$$

Thus, the time-scale for thermodiffusion is given by $t \sim \frac{k_b T L^2}{D_i Q_i^*}$, where k_b is the Boltzmann's constant. Using $Q_i^* \sim 0.1\ kJ/mol$ [10]gives t ~ 25000 s.

Derivation of Eqs. 2 and 3

$$I_1 = I + I_2 \tag{S1}$$

$$I_4 = I_5 + I \tag{S2}$$

$$V_2 - V_3 = I_3(R_{diff} + R_{soret}) \tag{S3}$$

$$I_2 = I_3 + I_1 \tag{S4}$$

$$I_3 + I_4 = I_5 \tag{S5}$$

$$V_1 - V_2 = I_2 R_{dl1} \tag{S6}$$

$$V_3 - V_4 = I_5 R_{dl2} \tag{S7}$$

$$-C_{dl1}\frac{d(V_1 - V_2)}{dt} = I_1 \tag{S8}$$

$$-C_{dl2}\frac{d(V_3 - V_4)}{dt} = I_4 \tag{S9}$$

Assuming that R_{diff} and R_{Soret} don't change within one oscillation, gives

$$-\left(\frac{I_1}{C_{dl1}} + \frac{I_4}{C_{dl2}}\right) = \frac{d(V_1 - V_4)}{dt} \tag{S10}$$

Substituting $f_1(t) = I_1/C_{dl1}$, and $f_2(t) = I_4/C_{dl2}$ gives Eq. 2.

$$I_2 = \frac{(V_1 - V_2)}{R_{dl1}} \quad \text{(S11)}$$

$$I_5 = \frac{(V_3 - V_4)}{R_{dl2}} \quad \text{(S12)}$$

Using Eqs. S8, S9, S10, and S11 gives

$$f_1(t)R_{dl1}C_{dl1} + \int f_1(t)dt = IR_{dl1} \quad \text{(S13)}$$

$$f_2(t)R_{dl2}C_{dl2} + \int f_2(t)dt = IR_{dl2} \quad \text{(S14)}$$

Adding Eqs. S13 and S14 give Eq. 3.

Effect of 'ionic mobility' on charging/discharging time-scales, voltage fluctuations during open circuit conditions, and oscillations during discharge

Thermal charging of TRECO devices: The thermal charging of TRECO, or for that matter any Soret-effect driven ionic thermoelectric generator, may be explained as follows:

1. Before applying the temperature gradient: Initially, before the TRECO device is placed in the setup depicted in Fig. 1a, there is no temperature difference across the TRECO electrodes. Since (i) TRECO is a symmetric device, both electrodes are made of the same material, and (ii) initially the ions are distributed uniformly (i.e., no concentration gradient), there is no ion separation, and, hence, no inherent voltage is expected in the absence of a temperature gradient (this can be seen from the negligible 9 mV OCV observed in Fig. 10b). An uniform initial ion distribution implies that, in Eq. 1, concentration gradients may be set to zero i.e.,

   $$\frac{\partial C_i}{\partial x} = 0 \quad \text{(S15)}$$

2. Initial phase after applying temperature gradient: As soon as the TRECO is placed in the setup held at a temperature difference ΔT depicted in Fig. 1a, the Soret effect kicks in so

that lighter ions (Na^+) accumulate near the hot electrode and the larger anions (ClO_2^-) accumulate near the cold electrode.[11] This in turn, is expected to induce opposite charges on the electrode surfaces, thus inducing the negative charges on the hot electrode and the positive charges on the cold electrode. Since, initially, concentration gradients before the start of this phase are negligible, this phase is largely governed by Eq. S16 shown below, which is derived by plugging in Eq. S15 into Eq. 1.

$$\frac{\partial C_i}{\partial t} = \frac{\partial}{\partial x}\left(\frac{D_i C_i Q_i^*}{k_b T^2}\frac{\partial T}{\partial x}\right) \tag{S16}$$

Since ion mobility is directly proportional to D_i, low ion mobility or diffusivity, is expected to enhance the charging time required for this initial phase.

3. Further thermal charging after the initial phase: After the Soret effect-induced ion separation has been achieved in the initial thermal charging phase, (charged) electric double-layers get formed at the electrode-electrolyte interfaces. As indicated in Fig. 1b, within the double-layers, the electrostatic attraction between oppositely charged ions and electrodes drives the ions towards the electrode via 'ionic migration', and Fick's diffusion tends to drive the ions away from the double-layer. Furthermore, since complete ion separation is not achieved in the initial phase, the Soret effect still tries to push the ions toward the electrodes. Hence, the Soret effect and Fick's diffusion are two ion transport mechanisms that push and pull the ions from and toward the bulk electrolyte. These above-mentioned phenomenon may be understood better via the following equations within the (a) bulk electrolyte and (b) electric double-layer at the electrode-electrolyte interfaces,

   a. *Bulk electrolyte*:

$$\frac{\partial C_i}{\partial t} = \frac{\partial}{\partial x}\left(D_i \frac{\partial C_i}{\partial x} + \frac{D_i C_i Q_i^*}{k_b T^2}\frac{\partial T}{\partial x}\right) \tag{S17}$$

$$\frac{\partial C_i}{\partial t} = D_i\left(\frac{\partial^2 C_i}{\partial x^2} - \frac{2C_i Q_i^*}{k_b T^3}\left(\frac{\partial T}{\partial x}\right)^2 + \frac{Q_i^*}{k_b T^2}\frac{\partial T}{\partial x}\frac{\partial C_i}{\partial x}\right) \tag{S18}$$

Since, ion mobility is directly proportional to ion diffusivity, low ion diffusivity effectively enhances the time-scale of each of the processes represented on the RHS of Eq. S18. The first term on the RHS of S18 represents Fick's diffusion which tends to drive ions towards the bulk electrolyte and hence can lead to

enhanced voltage fluctuations. So, low diffusivity/mobility helps to reduce voltage fluctuations. Furthermore, the next two terms on the RHS come from the Soret effect, and hence, low diffusivity/mobility enhances the time-scale required by the Soret effect to push ions toward the electrodes as well. Another point to note is that the Soret effect terms also depend upon ion concentration; hence, when the ion concentration within the bulk drops, the second term reduces in magnitude. The low ion concentration within the bulk indicates that most ions have been stored within the diffuse double-layer and diffusion layer close to the electrode-electrolyte interfaces. This essentially implies that concentration gradients are higher and Fick's diffusion fluxes driving ions towards the bulk electrolyte will be higher. Thus, essentially, this implies that at higher voltages (which arise from higher charge separation), more frequent voltage fluctuations may be expected if the diffusivity is high, and low diffusivity helps us prevent that to an extent.

b. *Electric double-layer:* Since the electric double-layer is usually very thin compared to the bulk electrolyte, an appreciable temperature difference is not expected across a few 'nm' thick double-layer. Furthermore, the double-layer is situated at the electrode-electrolyte interface, and the thermal resistivity of the insulating cellulose separator is expected to be much higher than that of the electrodes (which are ideally conducting). So, not just the temperature difference but even the temperature gradient within the electric double-layer is expected to be much lower. So, within the electric double-layer we neglect (a) the Soret effect/thermodiffusion, and (b) temperature associated variation in ionic mobility (D/RT). However, due to the high electric field within the electric double-layer, ionic migration is expected to be an additional flux mechanism that would be active within the electric double-layer, apart from Fick's diffusion.

Hence[12],

$$\frac{\partial C_i}{\partial t} = D_i \frac{\partial^2 C_i}{\partial x^2} + \frac{z_i D_i F c_i}{RT} \frac{\partial^2 \emptyset}{\partial x^2} + \frac{z_i D_i F}{RT} \frac{\partial c_i}{\partial x} \frac{\partial \emptyset}{\partial x}\ , \tag{S19}$$

$$\frac{\partial^2 \emptyset}{\partial x^2} = \frac{-F}{\varepsilon \varepsilon_0} \sum z_i c_i, \tag{S20}$$

where the relative dielectric constant of the electrolyte and the dielectric permittivity of the vacuum are given by ε and ε_0. Furthermore, $z, R, F, \emptyset$ represent the charge number, universal gas constant, Faradays' constant, and electrostatic potential. Equation S20 is Poisson's equation, which relates the electrostatic potential to the differences in ion concentrations of cations and anions within the electric double-layer (as z for cations and anions is +1 and -1, respectively, for our chosen salt: sodium chlorite).

Substituting Eq. S20 in Eq. S19 and assuming negligible cation concentration at the positive electrode-double-layer interface (at $x = 0$) , i.e., $c_c = 0$ at all times gives

$$\frac{\partial c_a}{\partial t} = D_a \frac{\partial^2 c_a}{\partial x^2} - \frac{D_a F^2 c_a^2}{RT \varepsilon \varepsilon_0} - \frac{D_a F}{RT} \frac{\partial c_a}{\partial x} \frac{\partial \emptyset}{\partial x} \qquad \text{at } x = 0, \tag{S21}$$

where subscript a indicates anion and subscript c indicates cation. Furthermore, a similar equation for cation concentration within the double-layer at the negative electrode-electrolyte interface (at $x = L$) is expected and has not been shown for simplicity. The first term on the RHS of Eq. S21 comes from Fick's diffusion, and the next two terms are related to ionic migration. Since each is directly dependent on diffusivity (and hence, ionic mobility), a lower diffusivity reduces migration and diffusion. Thus, it indirectly reduces both the charging rates and the voltage fluctuation frequency.

Hence, while lower diffusivities and ionic mobilities are expected to enhance charging time-scales, they also reduce the voltage fluctuation frequency during the thermal charging process and, thus, reflect two sides of the same coin.

Constant current discharge and oscillations

The effect of diffusivity/ionic mobility on discharge time-scales can be studied via its effect of voltage oscillations, as the presence/absence of oscillations is expected to significantly alter discharge time-scales.

We assume electroneutrality ($\sum z_i c_i = 0$) and negligible potential gradient at the double-layer-bulk electrolyte interface ($x = DL_+,\ DL_-$) which gives

$$\frac{\partial c_a}{\partial t} = 0 = \frac{\partial c_c}{\partial t} \quad \text{at } x = DL_+, DL_- \tag{S22}$$

This assumption is valid because electroneutrality is valid within the bulk electrolyte. In electric double-layer capacitors (TRECO is a type of electric double-layer capacitor), the highest potential gradient is present within the double-layer, and we have a negligible potential drop within the bulk electrolyte.

Furthermore, current density I at the electrode-electrolyte interface is given by[12]

$$I = \sum z_i F\left(-D_i \frac{\partial C_i}{\partial x} - \frac{z_i D_i F C_i}{RT}\frac{\partial \emptyset}{\partial x}\right) \tag{S23}$$

For constant current discharge,

$$\frac{dI}{dt} = 0 \tag{S24}$$

So, at the positive electrode- double-layer interface (at $x = 0$), where $c_c = 0$ at all times,

$$0 = F\left[D_a \frac{\partial}{\partial x}\left(\frac{\partial c_a}{\partial t}\right) - F\frac{D_a}{RT}\left(\frac{\partial c_a}{\partial t}\frac{\partial \emptyset}{\partial x} + c_a \frac{\partial}{\partial x}\left(\frac{\partial \emptyset}{\partial t}\right)\right)\right] \text{ at } x = 0 \tag{S25}$$

An order of magnitude analysis of Eq. S23 and assuming that $c_c = 0$ at $x = 0$ implies

$$I \sim \frac{F D_a c_a}{SL_+}\left(1 - \frac{F\emptyset}{RT}\right) \quad \text{at } x = 0, \tag{S26}$$

where SL_+ refers to the Stern layer thickness at the positive electrode-electrolyte interface. The SL_+ was used instead of the whole double-layer thickness as the assumption of $c_c = 0$ is expected to be valid only near the positive electrode-electrolyte interface and not within the whole double-layer.

The Stern layer thickness has been found to depend upon the surface potential, surface charge density, as depicted below,[12]

$$SL_+ \sim \frac{\varepsilon\varepsilon_0}{\sigma_{surf}}(\emptyset - \varsigma), \tag{S27}$$

where $\sigma_{surf}, \emptyset$, and ς represent surface charge density, electrostatic potential of the positive electrode surface $(x = 0)$, and electrostatic potential at the Stern-layer diffuse layer interface within the double-layer.

Additionally,

$$I = -\frac{d\sigma_{surf}}{dt}. \tag{S28}$$

Performing order of magnitude analysis on Eq. S28, and then using Eqs. S27-S28 in Eq. S26 gives,

$$\frac{-1}{T_d} \sim \frac{FD_aC_a}{\varepsilon\varepsilon_0(\emptyset-\varsigma)}\left(1 - \frac{F\emptyset}{RT}\right) \quad \text{at} \quad x = 0. \tag{S29}$$

where T_d is the discharging time scale. Furthermore, using Gauss's law at the positive electrode-electrolyte interface implies that

$$\frac{\partial\emptyset}{\partial x} = \frac{\sigma_{surf}}{\varepsilon_0(\varepsilon - \varepsilon_{electrode})} \quad \text{at } x = 0,\ ^{13} \tag{S30}$$

where $\varepsilon_{electrode}$ is the relative dielectric permittivity of the electrode. Using Eqs. S28, S30, along with the fact that $c_c = 0$ at $x = 0$ implies

$$-\frac{d\sigma_{surf}}{dt} = F\left(-D_c\frac{\partial C_c}{\partial x} + D_a\frac{\partial C_a}{\partial x} - F\frac{D_a C_a \sigma_{surf}}{RT\varepsilon_0(\varepsilon-\varepsilon_{electrode})}\right) \quad \text{at } x = 0. \tag{S31}$$

The first two terms of the RHS in Eq. S31 correspond to Fick's diffusion (in this case, Fick's diffusion wishes to drive the anions away from the positive electrode and cations away from the negative electrode towards the bulk and eventually the positive electrode). The last term of the RHS in Eq. S31 represents migration flux, which tends to drive the anions towards the positive electrode.

Let us suppose that to begin with the migration and Fick's diffusion terms are balanced, which automatically implies that the current is low (because if they are perfectly balanced, the current would be zero). However, if the current is very high, the terms related to Fick's diffusion and migration are automatically unbalanced to start with. Hence, we do not observe oscillations during discharge at very high currents before polarity reversal.

Furthermore, in cases where the current is low enough to allow oscillations during discharge before polarity reversal, at voltages where oscillations are observed

$$-D_c\frac{\partial C_c}{\partial x} + D_a\frac{\partial C_a}{\partial x} \sim F\frac{D_a C_a \sigma_{surf}}{RT\varepsilon_0(\varepsilon-\varepsilon_{electrode})} \text{ at } x = 0. \tag{S32}$$

At low/high σ_{surf} values, i.e., when the TRECO has been discharged/charged sufficiently, oscillations may be seen because, at low/high voltages, most of the ions would be present within the bulk electrolyte/double-layer. This implies that the concentration gradients would be low/high, and thus both the LHS (due to low/high concentration gradients) and RHS (due to low/high surface charges) of Eq. S32 go hand in hand. Thus, oscillations may even be seen at lower voltages if the discharge current is low enough to allow oscillations at higher voltages. Furthermore, suppose both cation and anion diffusivities have similar orders of magnitude. In that case, diffusivity just drops

out of Eq. (S32), and any dependence on diffusivities is only implicit (via the dependence of concentration profiles on diffusivities) and not explicit.

While the above explanation tells us that oscillations may also be seen at lower voltage magnitudes if the current allows oscillations at higher voltage magnitudes, the careful analysis below clarifies the role of current, voltage, temperature, and diffusivities/mobilities in governing the range of voltages at which oscillations may be observed. For galvanostatic conditions,

$$\frac{dI}{dt} = 0 \tag{S33}$$

Eqs. S28, S31-S33, and the fact that $c_c = 0$ at $x = 0$ at all times, together imply

$$\frac{\partial}{\partial x}\left(\frac{\partial c_a}{\partial t}\right) \sim \frac{F}{RT\varepsilon_0(\varepsilon-\varepsilon_{electrode})}\left(\frac{\partial c_a}{\partial t}\sigma_{surf} - c_a I\right) \text{ at } x = 0. \tag{S34}$$

Let us say voltage oscillations are present at a particular voltage V_{yes}. While Eq. S32 governs whether we observe oscillations or not, the continuous presence of oscillations at voltages in the neighborhood of V_{yes} is governed by Eq. S34 because the LHS and RHS represent rates of change of (a) diffusion fluxes and (b) migration fluxes, respectively. For oscillations to be present for an extended time period/voltage range (around the voltage where oscillations are observed, i.e., V_{yes}), the rate of change of diffusion and migration fluxes should be same. Furthermore, both LHS and RHS depend upon ion diffusivities indirectly via Eq. S21. Additionally, the rearrangement of Eq. (S34) yields

$$\frac{F}{RT\varepsilon_0(\varepsilon-\varepsilon_{electrode})} c_a I \sim \frac{F}{RT\varepsilon_0(\varepsilon-\varepsilon_{electrode})}\left(\frac{\partial c_a}{\partial t}\sigma_{surf}\right) - \frac{\partial}{\partial x}\left(\frac{\partial c_a}{\partial t}\right) \text{ at } x = 0. \tag{S35}$$

Clearly, RHS of Eq. S35 is directly dependent upon ion diffusivity/mobility via Eq. S21, but LHS does not depend explicitly on ion diffusivities/mobilities at a fixed current (there is some implicit dependence as ion concentration very close to the electrode surfaces, i.e., $x = 0$ may depend upon ion diffusivity). Thus 'continuity' of voltage oscillations in the neighborhood of V_{yes}, may be achieved only at appropriate diffusivities.

In summary, if the current is low enough to allow oscillations, (a) oscillations may be observed both at high and low voltages, and such voltages depend upon diffusivities only implicitly (if cation and anion diffusivities have similar orders of magnitude), and (b) continuity of voltage oscillations may be seen only at appropriate diffusivities. Thus, the effect of diffusivity/mobility on discharge time-scales is a complex issue if oscillations are present. However, if currents are high, and no oscillations are observed during discharge before flipping polarities, then the discharge time-scale is indirectly proportional to ion diffusivities, as per Eq. S29.

Movies:

SM1: Electric double-layer capacitor versus TRECO

SM2: PID controller induced fluctuations for stainless steel setup

SM3: Calculator powered using TRECO module- part 1

SM4: Calculator powered using TRECO module- part 2

SM5: Single large format TRECO cell powers a pocket calculator

SM6: Wearable TRECO armband

Role of electrode microstructure and porosity in governing TRECO performance

The porosity is related to the thermopower of the cell because porosity and pore size distribution define the electrode microstructure, which subsequently affects the way electric double-layers at various surfaces within the same electrode interact with each other. The charge distribution within the electric double-layer further governs the cell voltage which is related to charge separation and concentration profiles. For example, a typical double-layer (sublayers being the inner Helmholtz plane (IHP), outer Helmholtz plane (OHP), diffuse layer, and diffusion layer[14] where the IHP, OHP, and diffuse layer are non-electroneutral, and diffusion layer is electroneutral) thickness is ~ 1 nm. [14] If the pore sizes are also ~ 1 nm, then the double-layers created at two opposite surfaces of the same pore tend to overlap with each other, which further changes the ion concentration profile within the pore. Additionally, the double-layers might also overlap, if two shallow pores are situated very close to each other. This phenomenon has been depicted in the Fig S8.

Moreover, as is evident through Eqs. 2-3 and Eqs. S1-S14, and the confirming experimental data presented in Fig. 5, the oscillations arise due to the competition between Fick's diffusion and ion migration in the electric double-layer at the electrode-electrolyte interfaces. Since (as stated above) the typical thickness of electric double-layers is ~ 1 nm, and since the most dominant pore size for CD1 and CD2 is about 1-2 nm (Fig. 1c and Fig. S1), it is evident that the double-layer is contained within the pores and that double-layers at opposite surfaces of the pore might overlap and interact with each other. This affects the ion concentration distribution within the double-layer. Additionally, within nanoscale pores, ion-confinement effects might be activated[1516–18]. Thus, the diffusivity (which controls Fick's diffusion) and mobility (which controls the ionic migration) might be different from those within the bulk electrolyte far away from the electrode-electrolyte interfaces. Thus, porosity and electrode microstructure indirectly affect diffusion and migration, which further affect the oscillations.

So, both the novel effects ((a) high thermopower and (b) voltage oscillations) are directly governed by the electrode microstructure and porosity.

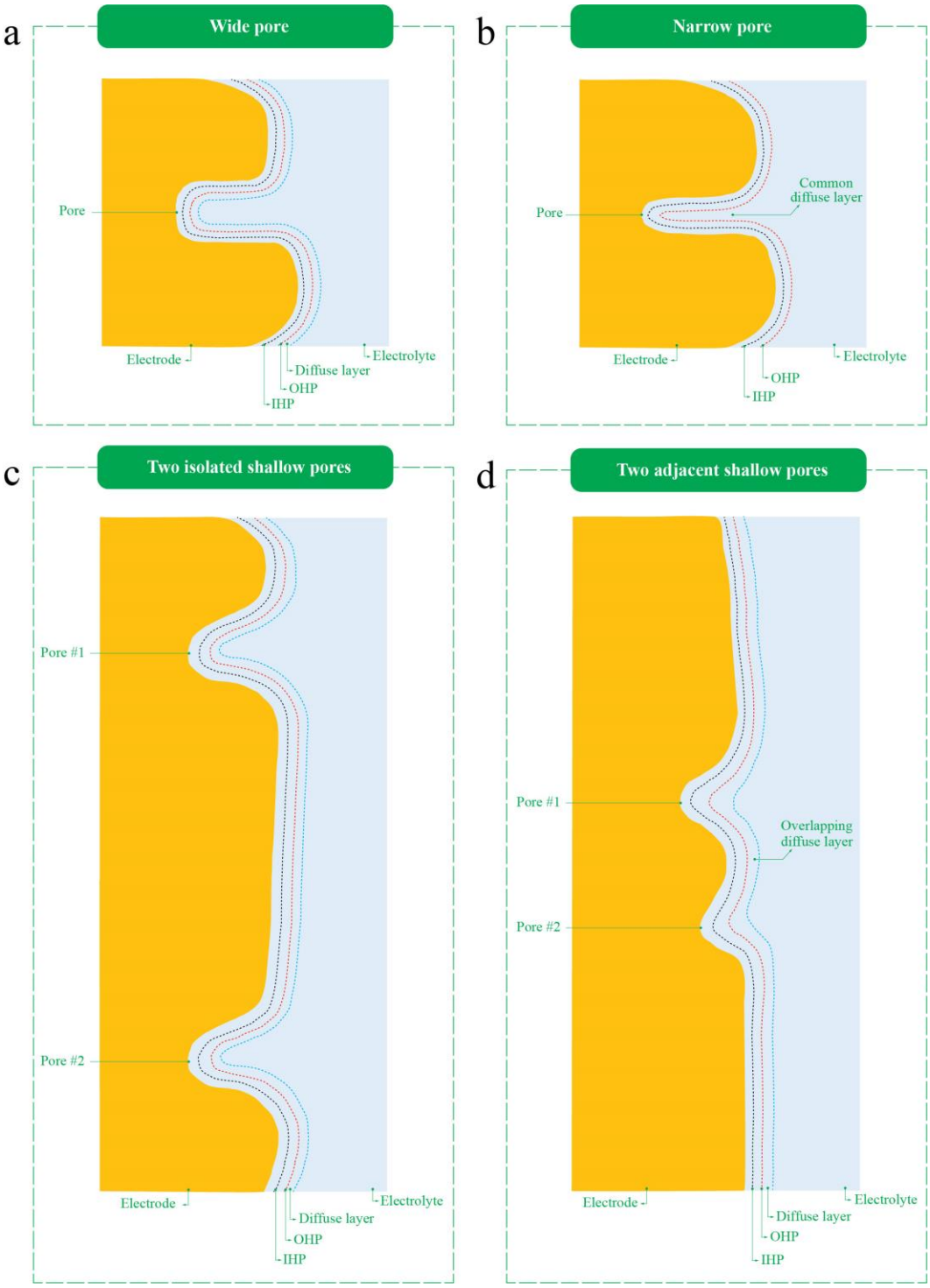

Figure S11: Effect of electrode microstructure and pore sizes on electric double-layer (EDL). (a) EDL inside a wide pore, (b) overlapping EDL inside a narrow pore, (c) non-overlapping EDL for isolated shallow pores, and (d) overlapping EDL for nearby shallow pores. For simplicity, we have not shown the electroneutral diffusion layer in any of the panels, as only the structure of non-electroneutral sub-layers is expected to affect the potential profile.

Discharging TRECO coin cells using a constant resistance load

We conducted additional experiments where a TRECO cell was charged thermally and then discharged by connecting it across different resistors. During discharge, two conditions were explored (with and without the temperature difference across the two electrodes). We once again observed voltage oscillations during discharge, both with and without the temperature difference across the electrodes. The total energy that was dissipated (and hence the total energy that was harvested and stored in the TRECO coin cell) in the resistors (100 kΩ, 75 kΩ, 50 kΩ, 25 kΩ, 10 kΩ, and 1 kΩ), without any temperature difference between the electrodes, was 11.76 mJ (or 3.27 μWh). Thus, the total energy that it stores is equivalent to energy that would be harvested within 2 hours if the harvested power was equal to the average power dissipated in the 100 kΩ resistor. Table S4 shows the energy dissipated and the average power for every resistor.

Table S4: Energy and power dissipated in each resistor during discharge without a temperature difference between the electrodes for a single TRECO coin cell.

Resistor (kΩ)	Energy dissipated (mJ)	Average power (μW)
100	0.4767	1.6050
75	0.4993	1.5701
50	0.4810	1.4064
25	0.3272	0.9915
10	7.5449	0.1008
1	2.4375	0.0098
Total Energy dissipated	11.7668 mJ or 3.27 μWh	

TRECO efficiency calculation

We performed additional experiments where we measured the short circuit current and maximum open circuit voltage. They were further used to calculate the output power.[19] The thermal power input into the TRECO cell was modeled as $kA\Delta T/L$, where k is the effective thermal conductivity

of the TRECO coin cell, A is the cross-sectional area, ΔT is the temperature difference between the hot and cold ends, and L is the cell thickness. Accurate input power calculation thus requires the accurate measurement of the effective thermal conductivity of the coin cell.

To accurately measure the effective thermal conductivity, we measured the power consumed by the resistive heater (used for heating the copper block in Fig. 1a) at a steady state for different input currents. For the measurements, the currents were once ramped up and then ramped down (similar data was obtained for both sets of measurements). The resistor power was then plotted against the temperature difference, and the slope was used to calculate the thermal conductance. However, some portion of the consumed resistor power in the above experiments was also lost to the environment due to convective and radiative losses. So, to accurately calculate the thermal power input into the TRECO coin cell, it is imperative to account for the convective and radiative losses. Similar measurements (to produce a power versus temperature difference curve) were performed for a cork, which is a good thermal insulator, to account for the convective and radiative losses. In other words, a cork was used instead of the TRECO coin cell (cf. Fig. 1a). Since the cork is a good thermal insulator, the power consumed by the resistor at steady state was deemed to be equal to the sum of convective and radiative losses for the setup. The above two measurements were used to calculate the thermal conductance of the TRECO coin cell, which was further used to calculate the thermal power input into the TRECO coin cell.

TRECO's efficiency was further calculated using two methods:

(a) Power efficiency using Open circuit voltage and Short circuit current [19]

The output and input powers were then used to estimate the cell efficiency, which was found to be approximately 0.0017% or 0.05% of the Carnot efficiency calculated as 1-T_L/T_H, where T_L and T_H are the temperatures of the cold and hot ends, respectively.

(b) Energy efficiency as a function of load using constant resistance loads

The energy efficiency was calculated using the following procedure[20]:

$$Q_{in} = \frac{\kappa}{L} A(\Delta T) t_{op} - \int_0^{t_{op}} I^2 R_{TRECO} dt, \quad \text{(S36)}$$

$$E_{out} = \int_0^{t_{op}} I^2 R_{load} dt \, , \quad \text{(S37)}$$

$$\eta_E\ (\%) = \frac{E_{out}}{Q_{in}} * 100, \quad \text{(S38)}$$

where E_{out} is the energy dissipated in the load resistor, R_{load} is the load resistance, I is the current flowing through the circuit, A is the cross-sectional area of the TRECO cell, κ is the thermal conductivity of the TRECO cell, L is the thickness of the TRECO cell, t_{op} is the device operation time, Q_{in} is the heat energy used to generate the Soret effect, R_{TRECO} is the resistance of the TRECO device (~1 GΩ), and ΔT is the temperature difference across the TRECO device (set to 10 K).

The efficiencies as a function of load resistance are presented in the table below

Table S5: Energy efficiency as a function of load resistance for TRECO

Load resistance	Efficiency (%)
100 kΩ	6.05E-4
75 kΩ	7.03E-4
50 kΩ	8.56E-4
25 kΩ	8.37E-4
10 kΩ	5.81E-3

As shown in Fig. 11, a comparison of energy efficiencies with other Soret effect-based ionic thermoelectrics leads us to conclude that TRECO's efficiencies are amongst the highest efficiencies reported in the literature for ionic thermoelectric generators. This once again confirms that the high voltage more than compensates for the low effective ionic conductivity and leads to high efficiencies.

Energy efficiency versus power efficiency:

While the power efficiency falls within the range of the energy efficiency for TRECO, we postulate that using energy efficiency may be more appropriate for devices such as TRECO or

any other ionic thermoelectric generator due to the time-lag between ‘electronic movement’ through the external circuit (i.e., current) and the ‘ionic movement’ through the electrolyte.

References

1. Zheng, T., Sabet, S. M. & Pilla, S. Polydopamine coating improves electromagnetic interference shielding of delignified wood-derived carbon scaffold. *J Mater Sci* **56**, 10915–10925 (2021).
2. Sabet, S. M. *et al.* Sulfurized Polyacrylonitrile Impregnated Delignified Wood-Based 3D Carbon Framework for High-Performance Lithium–Sulfur Batteries. *ACS Sustain Chem Eng* **11**, 2314–2323 (2023).
3. Yakopcic, C., Taha, T. M., Subramanyam, G. & Pino, R. E. Memristor SPICE Modeling. in *Advances in Neuromorphic Memristor Science and Applications* 211–244 (Springer Netherlands, Dordrecht, 2012). doi:10.1007/978-94-007-4491-2_12.
4. Robin, P., Kavokine, N. & Bocquet, L. Modeling of emergent memory and voltage spiking in ionic transport through angstrom-scale slits. *Science (1979)* **373**, 687–691 (2021).
5. Li, T. *et al.* Cellulose ionic conductors with high differential thermal voltage for low-grade heat harvesting. *Nat Mater* **18**, 608–613 (2019).
6. Wu, H., Fang, W.-Z., Kang, Q., Tao, W.-Q. & Qiao, R. Predicting Effective Diffusivity of Porous Media from Images by Deep Learning. *Sci Rep* **9**, 20387 (2019).
7. Andisheh-Tadbir, M., El Hannach, M., Kjeang, E. & Bahrami, M. An analytical relationship for calculating the effective diffusivity of micro-porous layers. *Int J Hydrogen Energy* **40**, 10242–10250 (2015).
8. Thermal conductivity. *http://hyperphysics.phy-astr.gsu.edu/hbase/Tables/thrcn.html* (2024).
9. https://www.matweb.com/search/datasheet_print.aspx?matguid=1336be6d0c594b55afb5ca8bf1f3e042. AISI Type 316L Stainless Steel, annealed sheet. *https://www.matweb.com/search/datasheet_print.aspx?matguid=1336be6d0c594b55afb5ca8bf1f3e042* (2024).

10. Gaeta, F. S., Perna, G., Scala, G. & Bellucci, F. Nonisothermal matter transport in sodium chloride and potassium chloride aqueous solutions. 1. Homogeneous system (thermal diffusion). *J Phys Chem* **86**, 2967–2974 (1982).
11. Köhler, W. & Morozov, K. I. The Soret Effect in Liquid Mixtures – A Review. *Journal of Non-Equilibrium Thermodynamics* **41**, (2016).
12. Chauhan, P. S. *et al.* Influence of electrolyte on the photo-charging capability of a ZnO–FTO supercapacitor. *J Mater Chem A Mater* **12**, 22725–22736 (2024).
13. de Souza, J. P., Levy, A. & Bazant, M. Z. Electroneutrality breakdown in nanopore arrays. *Phys Rev E* **104**, 044803 (2021).
14. Wu, J. Understanding the Electric Double-Layer Structure, Capacitance, and Charging Dynamics. *Chem Rev* **122**, 10821–10859 (2022).
15. Yang, Y. D., Moon, G. J., Oh, J. M. & Kang, I. S. Discrete and Continuum Analyses of Confinement Effects of an Ionic Liquid on the EDL Structure and the Pressure Acting on the Wall. *The Journal of Physical Chemistry C* **123**, 2516–2525 (2019).
16. Ziemys, A., Grattoni, A., Fine, D., Hussain, F. & Ferrari, M. Confinement Effects on Monosaccharide Transport in Nanochannels. *J Phys Chem B* **114**, 11117–11126 (2010).
17. Zaragoza, A. *et al.* Molecular dynamics study of nanoconfined TIP4P/2005 water: how confinement and temperature affect diffusion and viscosity. *Physical Chemistry Chemical Physics* **21**, 13653–13667 (2019).
18. Chiavazzo, E., Fasano, M., Asinari, P. & Decuzzi, P. Scaling behaviour for the water transport in nanoconfined geometries. *Nat Commun* **5**, 3565 (2014).
19. Hu, R. *et al.* Harvesting Waste Thermal Energy Using a Carbon-Nanotube-Based Thermo-Electrochemical Cell. *Nano Lett* **10**, 838–846 (2010).
20. Wang, H. *et al.* Ionic Thermoelectric Figure of Merit for Charging of Supercapacitors. *Adv Electron Mater* **3**, (2017).